Winter cooling in the northern Arabian Sea

S. Prasanna Kumar and T. G. Prasad

Physical Oceanography Division, National Institute of Oceanography, Dona Paula, Goa 403 004, India

The upper thermo-haline structure and the surface meteorological parameters of the central and eastern Arabian Sea during the inter-monsoon (April–May, 1994) and winter monsoon (February–March, 1995) periods, were analysed to understand physical forcing that leads to the observed high productivity during winter in the northern Arabian Sea. The weak northerly winds and increased solar insolation during the inter-monsoon period, led to the development of a highly stratified upper layer with warm sea surface temperature (SST) (29.5°C) and shallow mixed layer depth (MLD) (25 m). In contrast, during winter, the upper thermo-haline field showed a dramatic change, with cold SST (25°C) and deep MLD (100 m) in the north, though the winds were weak (5 ms^{-1}). The atmospheric forcing that leads to the observed changes in the upper layer of the ocean is a combination of enhanced evaporation under the influence of the dry continental air from the north brought by the prevailing northeasterly trades and reduction in the solar insolation. Subsequent cooling and convective mixing injects nutrients into the surface layers from the thermocline region, which in turn triggers the primary production.

IT is well known that during summer monsoon (June–September) upwelling is a dominant mechanism which triggers plankton bloom and results in extremely high productivity in the Arabian Sea[1,2]. In contrast, the spatial variation in the productivity during winter (November–February) is less studied. On the basis of analysis of published data, Banse[3] inferred that the central Arabian Sea is more productive than subtropical gyre elsewhere, and the area north of 20°N to be richer than the central Arabian Sea. Our results from a recent Indian Joint Global Ocean Flux Studies (JGOFS) cruise, during February–March 1995, revealed the evidence of high productivity in the northern Arabian Sea, the details of which are presented elsewhere, in this issue[4]. In this article, we analyse the upper thermo-haline structure and the physical forcing that lead to the observed high productivity.

Data and methods

As a part of the Indian JGOFS programme, 36 CTD (Conductivity Temperature Depth) profiles were collected at one degree interval (up to 1000 m depth) onboard ORV *Sagar Kanya* during 4 February to 4 March 1995 (Figure 1 *a*). In accordance with the JGOFS protocol[5], Sea-Bird Electronics CTD was used to obtain temperature and salinity profiles. CTD salinities were calibrated against water samples collected simultaneously by a rosette sampler and analysed with a Guildline 8400 Autosal. The conversion of conductivity to salinity was made using the modified UNESCO formula[6]. The data collected during the JGOFS cruise of 14 April to 14 May, 1994 (Figure 1 *b*) were also utilized to highlight the changes in the water column. Apart from the CTD profiles, surface meteorological parameters were also collected during both the cruises. The surface meteorological observations on a $2° \times 2°$ grid from the Comprehensive Ocean Atmosphere Data Set[7] (COADS) were used to obtain monthly mean values of surface heat flux and evaporation. The surface fluxes (Wm^{-2}) were calculated using standard bulk aerodynamic formulae[8] for latent (Q_e) and sensible (Q_h) heat exchange:

$$Q_e = \rho L C_e (q_s - q_a) U,$$
$$Q_h = \rho C_p C_s (T_s - T_a) U,$$

where L is the latent heat of vaporization, C_p the specific heat of water, q the specific humidity, C_e and C_s the empirical exchange coefficients, T_s the sea surface temperature, T_a the air temperature, U the wind speed. The evaporation is computed by using the equation

$$E = \rho C_e (q_s - q_a) U.$$

The precipitation data were obtained from the Very High Resolution Radiometer (VHRR) onboard the INSAT (see ref. 9 for details). From these data, monthly mean precipitation on a $2° \times 2°$ grid was generated. Further, monthly values of evaporation–precipitation (E–P) were computed along 64°E.

Results

To understand the physical process, we analysed the observed surface wind as well as the vertical structure of temperature, salinity and sigma-*t* along the 4 legs (Figure 1).

Winds

The surface winds during February–March (Figure 2 *a*) were predominantly north/north-easterlies with occasional north-westerlies. Along the shelf, the observed

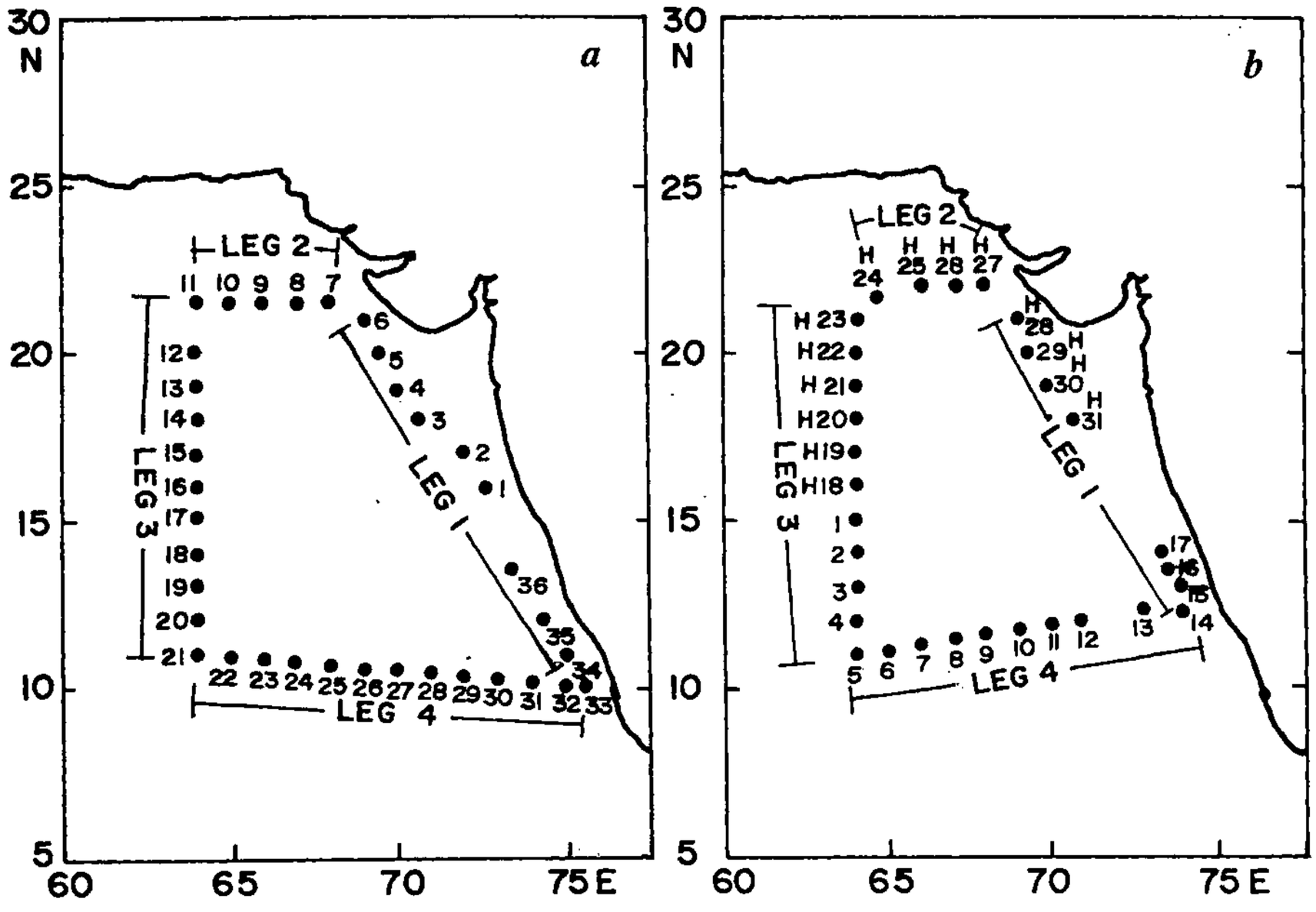

Figure 1 *a*, *b*. Location map of CTD stations occupied during (*a*) 4 February to 4 March (winter monsoon) 1995 and (*b*) 14 April to 14 May (inter-monsoon) 1994. H indicates profiles taken with hydrocast.

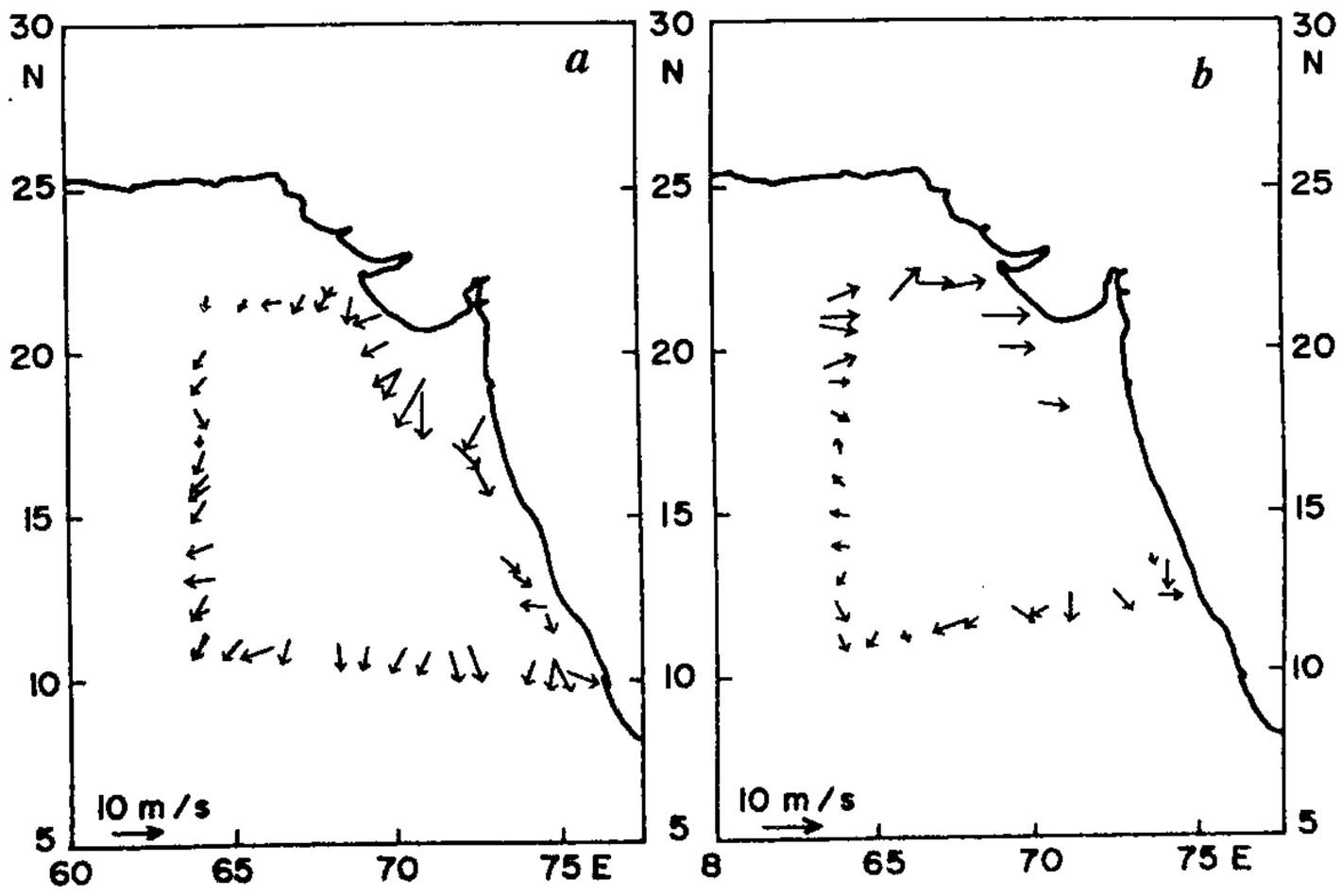

Figure 2 *a*, *b*. Wind vector during (*a*) winter monsoon, (*b*) inter-monsoon.

wind speed varied between 4 and 7 ms^{-1}, except at 18°N where it was about 12 ms^{-1}. In the open ocean, the wind speed showed a gradual increase from about 2 ms^{-1} to 5 ms^{-1} towards south. During April–May (Figure 2 *b*) the surface winds south of 17°N were predominantly northerly and weak (<4 ms^{-1}), but became progressively stronger towards north. Along the northern shelf, the wind speeds were between 8 and 10 ms^{-1}, decreasing to 6 ms^{-1} towards south. In the open ocean, wind speeds were high north of 18°N reaching up to 8 ms^{-1}.

Thermo-haline characteristics

Winter monsoon (February–March)

The thermal structure during February–March, along the shelf (leg 1), (Figure 3, top panel) showed a weakly stratified surface layer extending to 100 m depth, and the sea surface temperature (SST) rose from about 24.2°C in the north (21.5°N) to about 29°C at 10°N, approximately 0.5°C increase per degree latitude. The mixed layer depth (MLD), in general, was deep varying between 120 m at 21°N and about 80 m at 10°N. The packed isotherms below 100 m, along the southern shelf, indicated a strong thermocline. Salinity structure (Figure 3, bottom panel) also showed a weakly stratified layer of high salinity (36.4 PSU), in the north, thinning towards south. The very low salinity waters (< 34.6 PSU) towards south indicate the influence of the Bay of Bengal waters, being carried along the shelf by northward flowing coastal current. The high salinity surface waters (36.4 PSU) in the north is the Arabian Sea High Salinity Water mass (ASHSW), the core of which deepens towards south (about 100 m depth) and was identified by the 36.0 PSU isohaline.

Along 64°E (leg 3), the thermal structure showed a weakly stratified surface layer extending to 100 m depth, as seen along the shelf, with colder waters (<25°C) north of 17°N, while south of it, the SST increased to 27°C (Figure 4, left panel). Thermal structure depicts deep mixed layer in the north (21.5°N) which shoals to about 80 m at 20°N and once again deepens to 125 m at 17°N. South of 17°N, mixed layer depth shoals steadily, reaching up to 65 m at 11°N. Isotherms below the upper thermocline showed considerable shoaling towards south giving rise to strong gradient in the lower thermocline as well. This thermal structure essentially reflects the zonal flow pattern in the open ocean circulation. Below 500 m, the waters are well stratified with no appreciable north–south variation. Salinity structure (Figure 4, middle panel) showed the presence of ASHSW near the surface (> 36.4 PSU) in the northern region, the core of which deepens towards south. The surface salinity decreased from 36.4 PSU in the north to less than 35.7 PSU at 11°N. This low salinity water is the indication of North Equatorial Current (NEC), which carries along with it the low salinity waters from the Bay of Bengal as well as the eastern Indian Ocean into the western Arabian Sea during this season. The second subsurface high salinity (36.0 to 36.2 PSU) seen between 200 and 400 m in the north and spreading southward is the Persian Gulf water mass, which was also seen spreading eastward along leg 2. As it moves southwards beyond 14°N, the water mass loses its identity due to mixing with the Red Sea water mass, normally encountered south of 13°N, between 400 and 80 m depth and sigma-*t* 27.0, which is manifested by the thick isohaline layer between 200 and 800 m depth near 11°N. The sigma-*t* structure (Figure 4, right panel) mainly reflects the combined effects of thermo-haline structure. In the northern region, sigma-*t* greater than 24.5 was encountered at the surface with thick isopycnal layer (100 m), which gradually decreases southward and becomes as low as 22.0

The MLD along the zonal section (nominally along 10°N, leg 4), increased gradually from about 50 m in the west to almost 100 m towards the east with SST in general, warmer than 28°C (Figure 5, left panel). The packed isotherms in the upper 300 m indicate the signature of the NEC active during the winter monsoon. The presence of NEC brings about drastic changes in the surface salinity along this section (Figure 5, right panel) with very low salinity waters (34.6 PSU) from the eastern side over-riding the high salinity waters of the west. The core of the ASHSW (36.0 PSU) consequently showed an eastward deepening. The thick isohaline layer between 200 and 1000 m (which thins towards east), once again is the admixture of Persian Gulf and Red Sea waters.

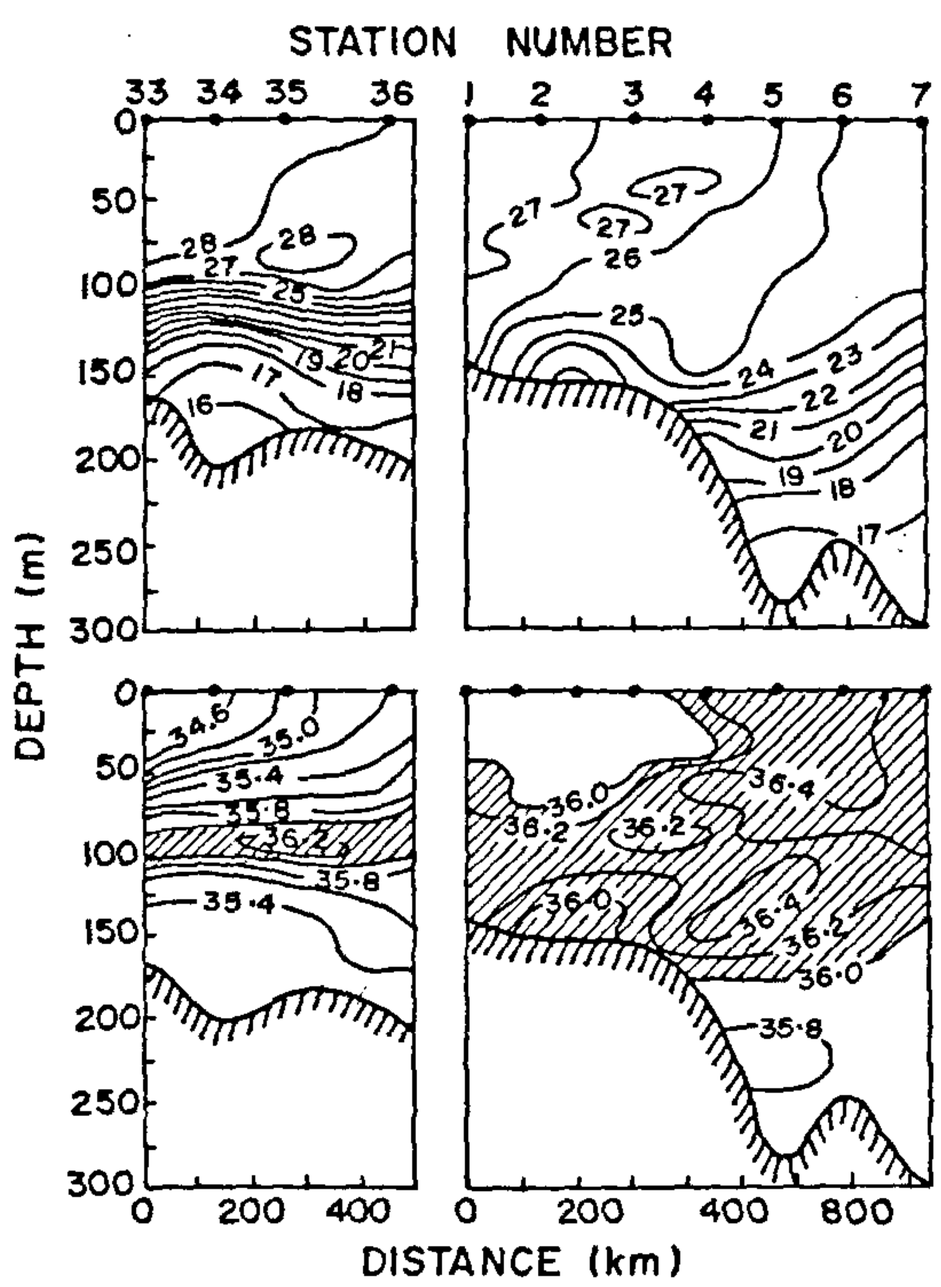

Figure 3. Vertical section of temperature (*top*) and salinity (*bottom*) along the shelf during winter monsoon. Salinity >36 PSU is hatched to demarcate the Arabian Sea High Salinity Water mass.

Inter-monsoon (April–May)

Along the western shelf (leg 1), thermal structure

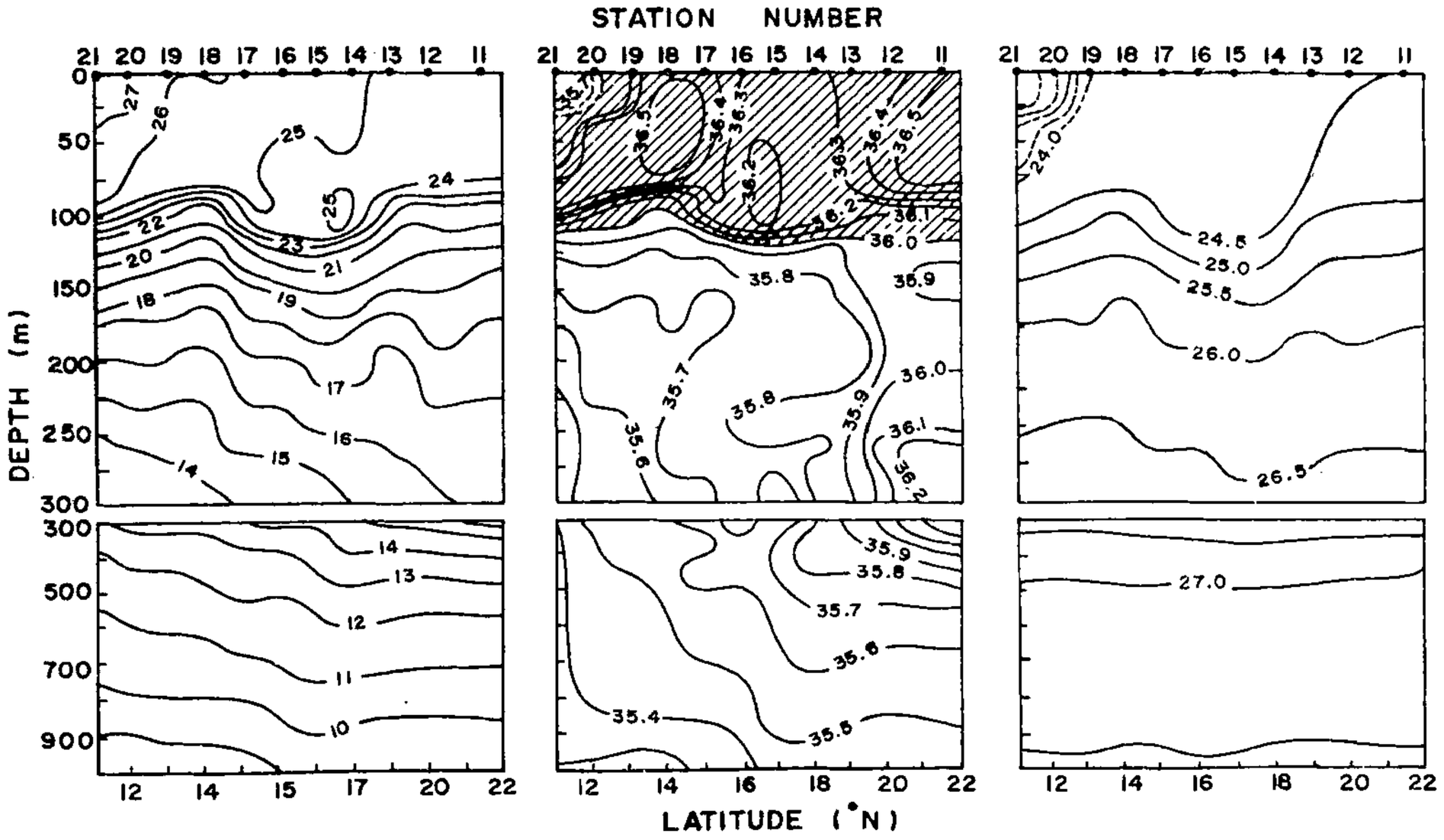

Figure 4. Vertical section of temperature (*left*) salinity (*middle*) and sigma-*t* (*right*) along 64°E during winter monsoon. Salinity >36 PSU is hatched to demarcate the Arabian Sea High Salinity Water mass.

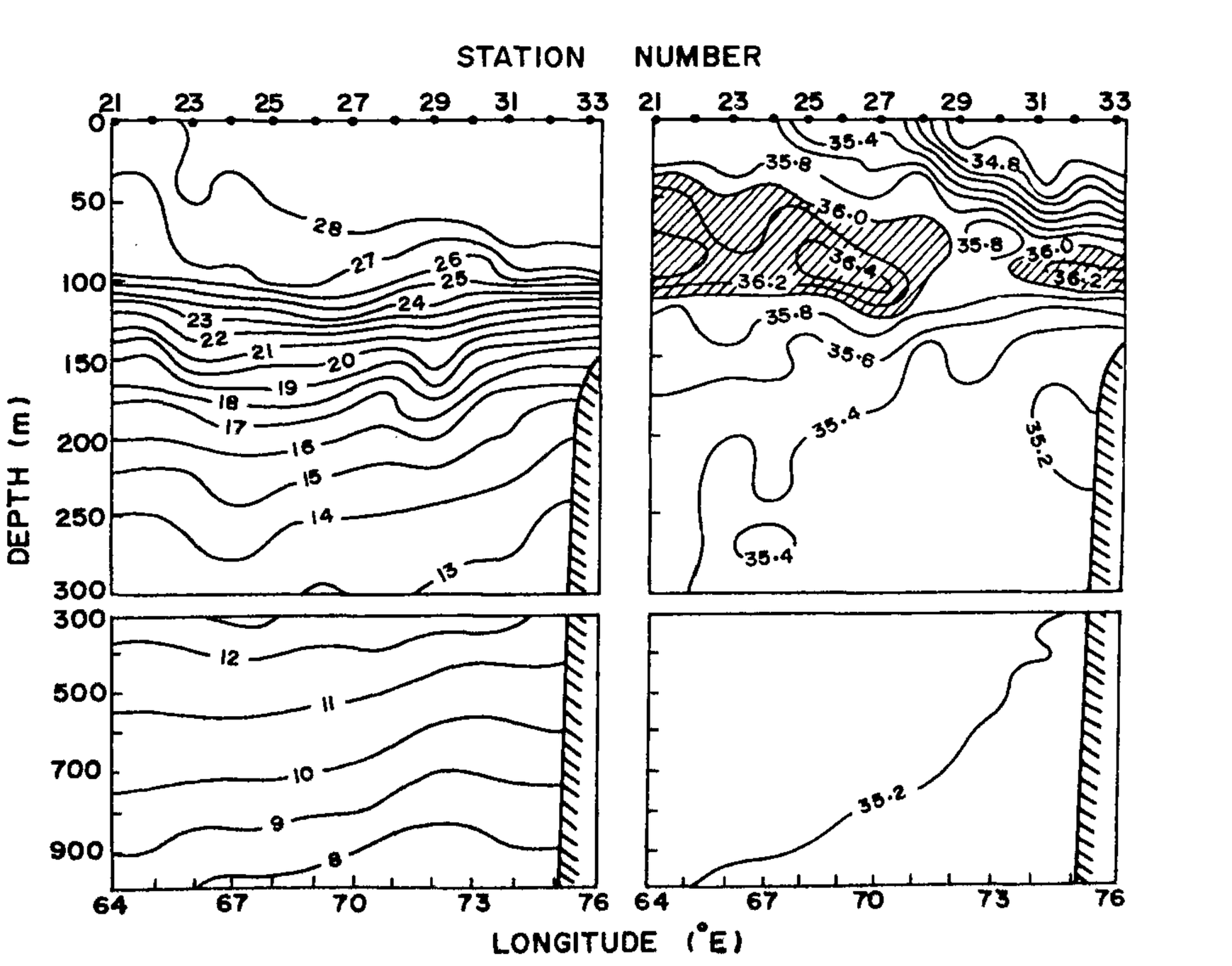

Figure 5. Vertical section of temperature (*left*) and salinity (*right*) nominally along 10°N during winter monsoon. Salinity >36 PSU is hatched to demarcate the Arabian Sea High Salinity Water mass.

showed thin mixed layer, varying marginally from 10 m in the north to 25 m in the south, with SST more than 30°C (Figure 6, top panel). More or less uniformly thick, high salinity waters (36.4 PSU) are encountered along the northern shelf, north of 16°N (Figure 6, bottom panel). However, along the southern shelf, low salinity waters are seen in the upper 20 m. The core of the ASHSW, which is seen almost at the surface in the north, deepens to about 80 m towards south.

The thermal structure along 64°E (leg 3) showed a well-stratified surface layer. The upper thermocline showed an overall trend of deepening from 21°N to 11°N, except between 13.5°N and 15.5°N where isotherms greater than 20°C shoals, appear to be a signature of a meso-scale (cold core) eddy (Figure 7, left panel). The MLD remained thin showing a general deepening, though small, toward south as in the case along the western shelf (leg 1). Salinity structure resembled that during February–March, except for the reduced spatial extent of the low salinity water in the southern region (Figure 7, middle panel). The thick isohaline layer seen in the north, during February–March, is no longer present. Instead, the high salinity (36.6 PSU) protrudes into the water column, indicating the spreading and deepening of the ASHSW towards south. Unlike during February–March, the sigma-*t* structure showed the presence of low density waters uniformly throughout from 21°N to 11°N (Figure 7, right panel) and strong stratification. The 24.5 isopycnal seen at the surface in the north during winter monsoon is not encountered at 60 m.

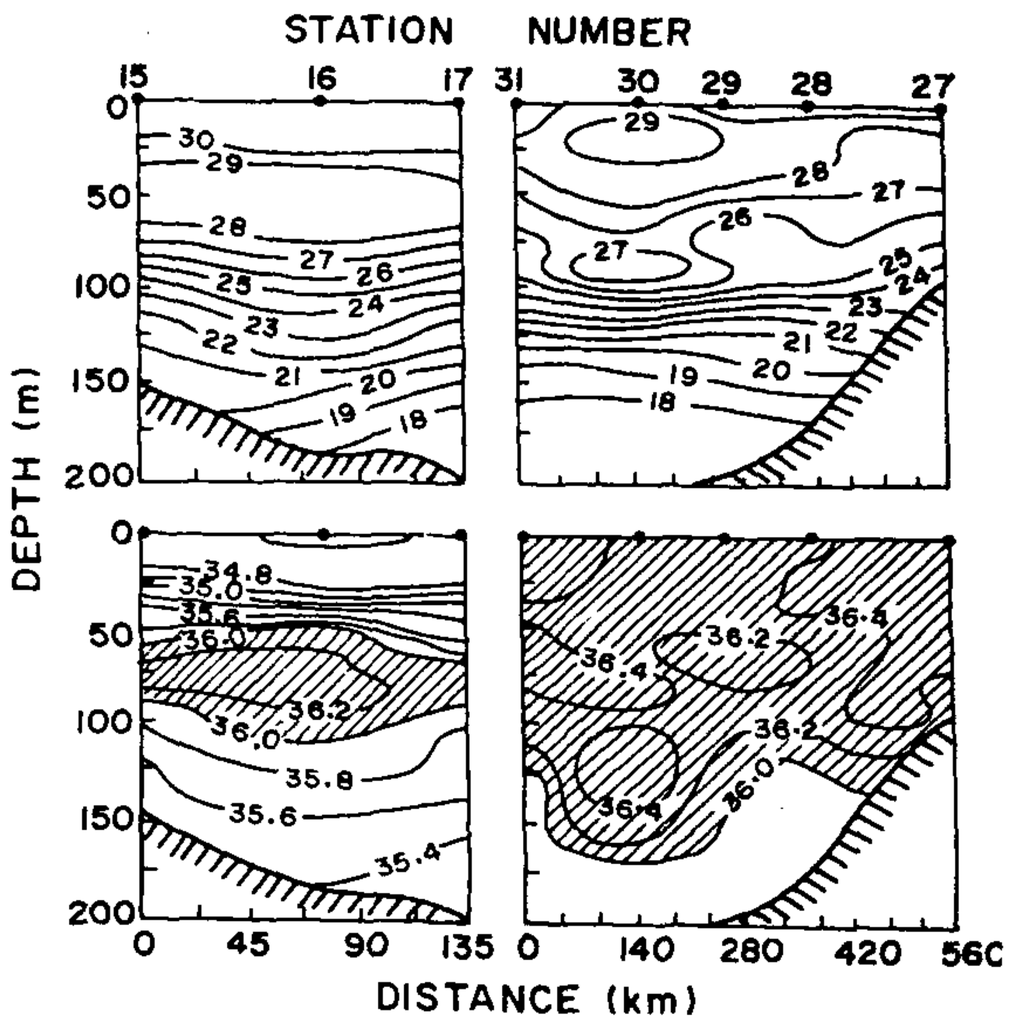

Figure 6. Vertical section of temperature (*top*) and salinity (*bottom*) along the shelf during inter-monsoon. Salinity >36 PSU is hatched to demarcate the Arabian Sea High Salinity Water mass.

Along leg 4 (nominally along 10°N), thermal structure showed extremely shallow MLD in comparison with February–March with the mixed layer temperature

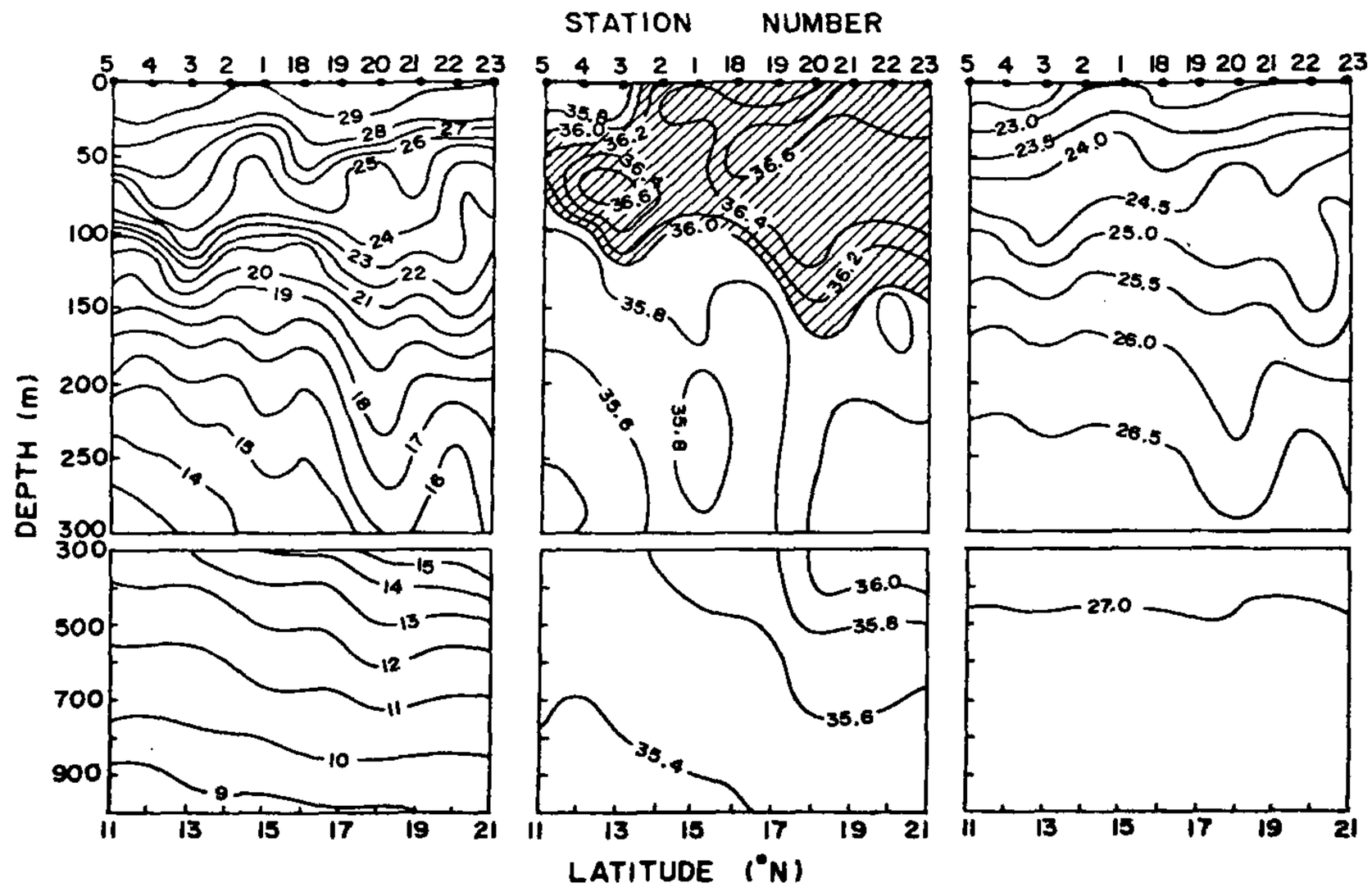

Figure 7. Vertical section of temperature (*left*) salinity (middle) and sigma-*t* (*right*) along 64°E during inter-monsoon. Salinity >36 PSU is hatched to demarcate the Arabian Sea High Salinity Water mass.

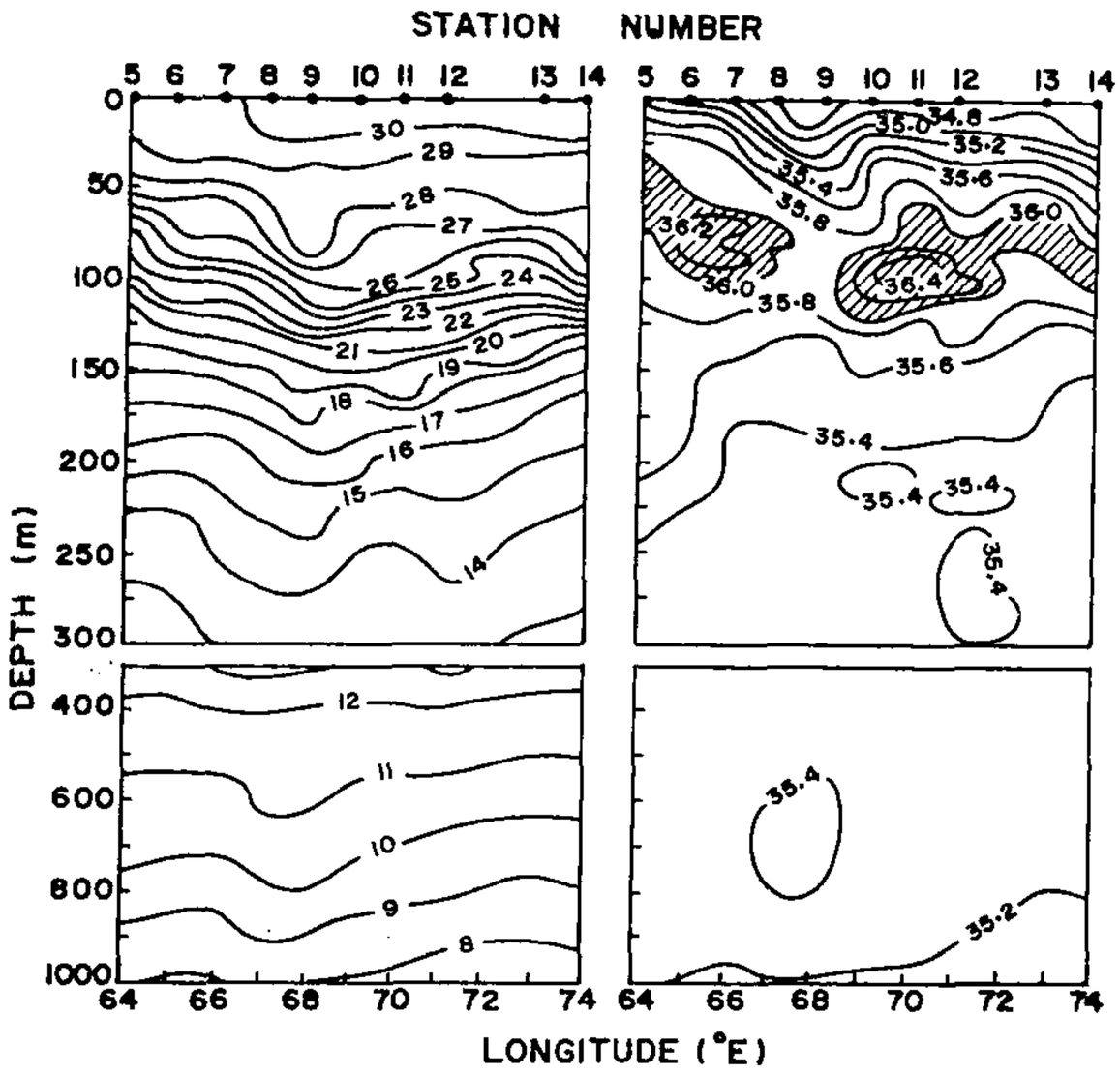

Figure 8. Vertical section of temperature (*left*) and salinity (*right*) nominally along 10°E during inter-monsoon. Salinity >36 PSU is hatched to demarcate the Arabian Sea High Salinity Water mass.

at least 2°C warmer (Figure 8, left panel). Though, in general the salinity structure was similar to that during February–March, the haline gradient seen at the eastern region is diffused (Figure 8, right panel). The thickness of the ASHSW also showed considerable change.

Surface meteorological parameters

To highlight the changes of the top layer of the ocean during winter monsoon, we over-plotted the air temperature, SST and MLD of inter-monsoon period along 64°E (leg 3).

The air temperature, during winter monsoon, increased from 23°C in north to a little more than 26°C in the south, while it was, in general, more than 28°C during inter-monsoon, and at times reached up to 30°C (Figure 9 *a*). The SST showed about 3°C rise from north (25°C) to south, in winter as compared to 1°C rise in inter-monsoon (Figure 9 *b*). The MLD during winter was deep (100 m) in the north (Figure 9 *c*), which shoals up to 80 m at 20°N and once again deepens to 120 m at 17°N. South of this MLD shoals steadily reaching up to 65 m. In comparison to winter monsoon, MLD was very shallow, varying between 10 m in the north and 35 m towards south, during inter-monsoon.

To understand the atmospheric forcing that lead to the observed changes in the upper thermo-haline fields, we analysed the heat and fresh water (evaporation–precipitation) fluxes along 64°E.

The time-latitude distribution of the latent heat flux along 64°E showed two high values, one during November–January, specially north of 10°N (130 Wm^{-2}), and the other during May–August (220 Wm^{-2}) in the central Arabian Sea (Figure 10 *a*). The sensible heat flux showed heat gain in the central Arabian Sea from June

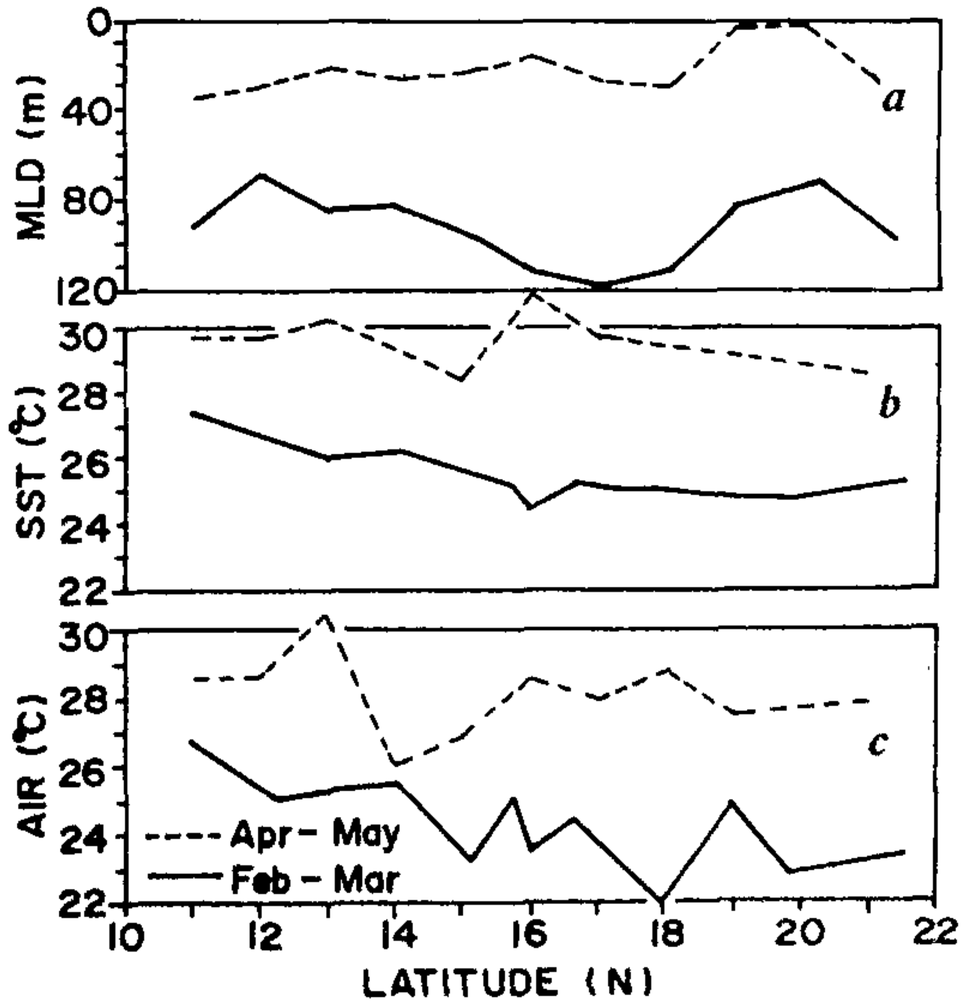

Figure 9 *a–c*. Distribution of (*a*) air temperature, (*b*) SST and (*c*) MLD. The solid line indicates winter monsoon and broken line inter-monsoon.

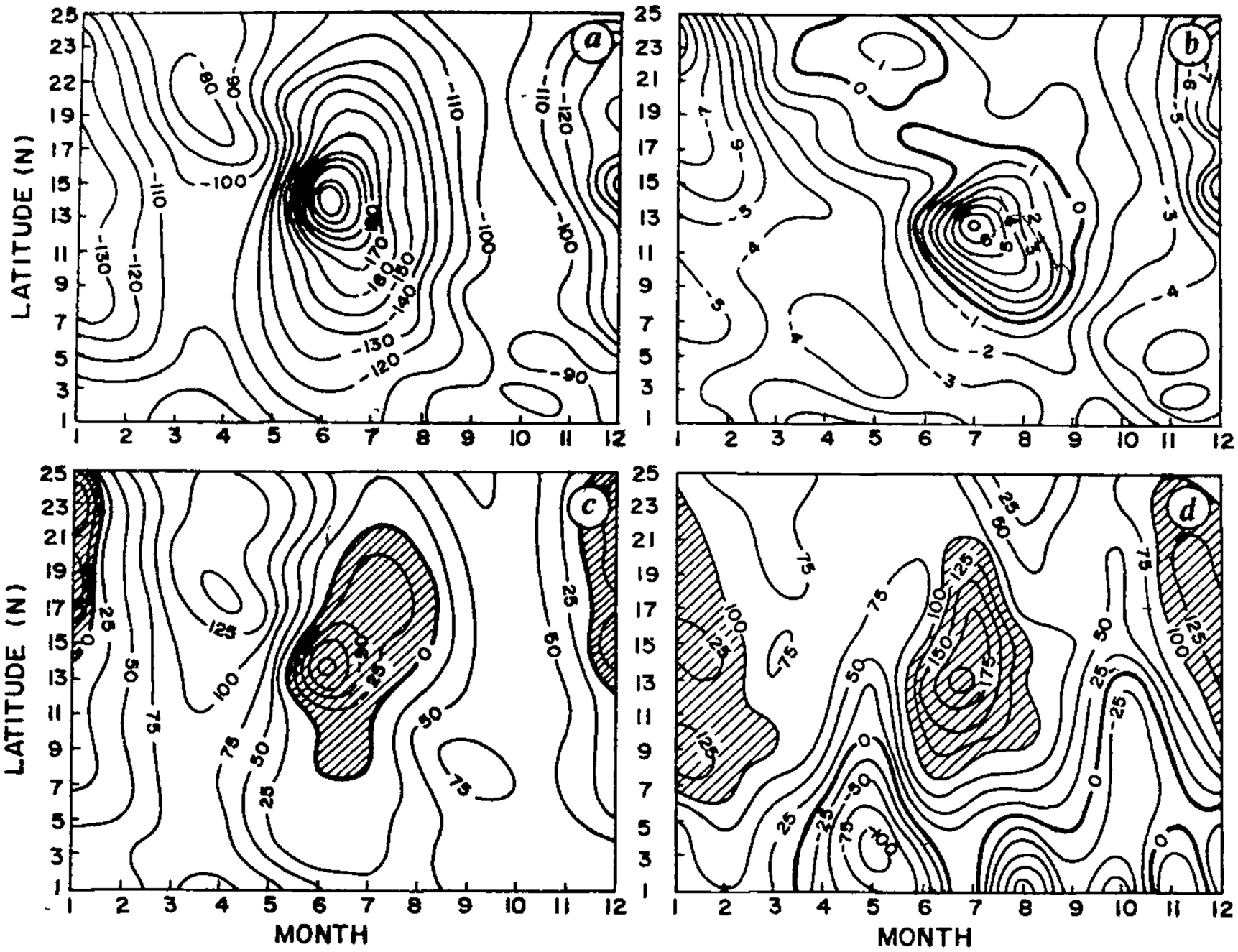

Figure 10 *a–d*. Time-latitude section of (*a*) Latent heat flux (Q_e, Wm^{-2}), (*b*) Sensible heat flux (Q_h Wm^{-2}), (*c*) Net heat flux (Wm^{-2}), and (*d*) evaporation–precipitation (E–P, mm/month) along 64°E. The hatched region in (*c*) represents a net heat loss while that at (*d*) shows where evaporation exceeds precipitation by more than 100 mm/

to September, while the northern Arabian Sea experienced significant heat loss during winter monsoon (about 7 Wm^{-2}, Figure 10 *b*). The net heat flux (Figure 10 *c*) pattern was similar to that of latent heat flux. E–P depicted a net fresh water loss north of 12°N, with two distinct maxima, one in summer (200 mm/month) and the other in winter (125 mm/month) monsoons (Figure 10 *d*). Throughout the year, the equatorial region receives excess precipitation over evaporation.

Discussion

The above analysis of the upper thermo-haline structure and the surface meteorological parameters brings out the interesting changes from winter monsoon to inter-monsoon as well as the predominant north–south variations. The thermal structure during April–May showed a thin mixed layer, varying from 20 to 35 m, with SST more than 29°C. The core of the ASHSW, seen below the surface in the north, deepens while spreading towards south. Unlike this, during February–March, the thermo-haline structure showed considerable changes in the upper layers. The most dramatic change takes place in the mixed layer, which becomes deeper than 90 m in the north, reaching up to 120 m at 17°N, while towards south it is shallower (about 65 m). A weakly stratified upper layer was observed, both along the shelf as well as in the open ocean. The surface meteorological conditions during April–May showed predominantly weak northerly winds south of 17°N, which becomes progressively westerlies and stronger towards the north. This indicated the prevalence of north-east monsoon conditions south of 17°N, and setting in of south-west monsoon north of it (Figure 2 *b*). The increase in SST (>29.7°C) over the air temperature (on an average 28°C) indicated the increasing solar insolation during this period (Figure 9 *a*), making the upper layer of the ocean highly stratified. Under the prevailing weak wind conditions and increasing solar insolation, one expects a rather thin and more or less uniform MLD as observed (Figure 9 *c*). During February–March, the winds were weak throughout, on an average 5 ms^{-1}, and were predominantly north/north-easterly indicating the prevailing winter monsoon conditions (Figure 2 *a*). North of 17°N, the air temperature (Figure 9 *a*) was very low (23°C) and accordingly the SST (Figure 9 *b*) also was

low (25°C). However, south of 17°N, conditions were warmer. Under the weak wind conditions, one would expect shallow MLD, as is the case during April–May. In contrast, the thermal structure showed deep MLD (Figure 9 *c*), specially north of 17°N in the open ocean. This suggests that the deepening of mixed layer in the north, during winter, is not due to wind but is driven by other atmospheric forcings.

In order to probe this further, we computed the heat and fresh water flux into the atmosphere (E–P) along 64°E. During winter the northern Arabian Sea (especially north of 10°N) experiences a net heat loss (about 140 Wm^{-2}). This value is slightly lower than that of Hastenrath and Lamb[10] which showed a net oceanic heat loss about 160 wm^{-2} from October to December. An examination of the climatological values[10] of specific humidity during October (19 g kg^{-1}) and January (about 10 g kg^{-1}) in the northeastern Arabian Sea indicates the prevalence of dry air during winter. The cool dry continental air brought into the northern Arabian Sea by the prevailing north-east trade winds enhances evaporation, as evident from E–P values (Figure 9), leading to surface cooling. We estimated the cooling due to loss of heat to the atmosphere using the formula[11] $\Delta T=Qt/CM$ [where Q is the net heat flux to the atmosphere (Wm^{-2}), t the time period (seconds) over which the heat flux occurs, C the specific heat of water ($4.18 \times 10^3 J\,kg^{-1}\,K^{-1}$) and M the mass (kg) of the water cooled], which works out to be about 3°C. Apart from the cooling due to evaporation, the decrease of solar insolation (net short wave radiation) from 220 Wm^{-2} during October to about 160 Wm^{-2} during January[10] also contributes to the further cooling of the surface waters. Thus, in short the observed reduction in SST (by about 4°C) and deep MLD, in the northern Arabian Sea during winter is forced by a combination of enhanced evaporation and reduction in the solar insolation. In fact, this starts during December and persists till end of February. Accordingly, the northern Arabian Sea, north of 15°N, experiences cooling and densification (Figures 4 and 7). This leads to the formation of ASHSW[12], sinking and convective mixing; and injects nutrients into the surface layers from the thermocline region, as is evident from the shoaling of 2 μM nitrate contour, which is seen at 30 m at 13°N and surfaced at about 17°N (ref. 13). In the Arabian Sea, nitrate in the surface layers is below detection level except during monsoonal upwelling. The nutrient injection to the upper layers of the water column triggers the primary productivity which was about 807 mg C m^{-2} per day[4]. On the basis of coastal zone colour scanner data, Banse and McClain[14] deduced the occurrence of highest pigment concentrations north of 20°N. The data presented here is the first ever observational evidence elucidating the physical forcing that brings about the winter bloom in the northern Arabian Sea.

1. Banse, K., *Deep-Sea Res.*, 1987, **34**, 713–723.
2. Qasim, S.Z., *Deep-Sea Res.*, 1982, **29**, 1041–1068.
3. Banse, K., in *Marine Geology and Oceanography of Arabian Sea and Coastal Pakistan* (eds Haq, B. U. and Milliman, J. D.), Van Nostrand Reinhold Co, New York, 1984, pp. 271–303.
4. Bhattathiri, P. M. A., Aditi Pant, Surekha Sawant, Gauns. M., Matonkar, S. G. P. and Mohanraju, R., *Curr. Sci.*, 1996, **71** (this issue).
5. Protocols for the JGOFS core measurements UNESCO, IOC, 1994.
6. Anonymous, *UNESCO Technical Paper in Marine Sciences, UNESCO*, 1981, vol. 37, pp. 144.
7. Woodruff, S. D., Slutz, R. J., Jenne, R. L. and Steurer, P. M., *Bull. Am. Meteorol. Soc.*, 1987, **68**, 1239–1250.
8. Bunker, A. F., *Mon. Weath. Rev.*, 1976, **104**, 1122–1140.
9. Ramesh Kumar, M. R. and Prasad, T. G., *J. Geophys. Res.*, 1996 (in press).
10. Hastenrath, S. and Lamb, P., *Climatic Atlas of the Indian Ocean. Part I: Surface Climate and Atmospheric Circulation*, The University of Wisconsin Press, Wisconsin, 1979.
11. Anthes, R. A., *Tropical Cyclones: Their Evolution, Structure and Effects, Meteorological Monographs*, 1982, vol. 19, pp. 208.
12. Prasanna Kumar, S. and Prasad, T. G., *Deep-Sea Res.*, 1996 (in press).
13. De Souza, S. N., Dileep Kumar, M., Sardesai, S. D., Sarma, V. V. S. S. and Shirodkar, P. V., *Curr. Sci.*, 1996, **71** (this issue).
14. Banse, K. and McClain, C. R., *Mar. Ecol. Progr. Ser.*, 1986, **34**, 201–211.

ACKNOWLEDGEMENTS. We thank the Director, National Institute of Oceanography for encouragement. Financial support for this study was provided by the Department of Ocean Development under the JGOFS (India) programme. We thank A.M. Almeida, M.T. Babu and Fernando Vijayan for their help in the data collection and Chitari for preparing the diagrams. This is NIO contribution no. 2503.